

Simulation package for solving dynamic diffraction problems in deformed crystals using beam propagation method.

Examples: Bragg, Laue geometry, asymmetric reflections, bend crystals, dislocations, crystals with arbitrary shapes and strain distributions and time dependent problems

Jacek Krzywinski^{a,b} and Aliaksei Halavanau^a

^aSLAC National Accelerator Laboratory, 2575 Sand Hill Road , Menlo Park CA 94025, USA

^bNational Centre for Nuclear Research, Otwock-Świerk, ul. A. Sołtana 7, Poland

ABSTRACT

We demonstrate the use of the Fast Fourier Transform Beam Propagation Method (FFT BPM) to simulate dynamic diffraction effects, including scattering from deformed crystals with arbitrary shapes in Bragg, Laue, and asymmetric geometries. The method's straightforward algorithm, combined with FFT, enables fast computation and is easy to implement in Python. It successfully reproduces literature results for bent crystals, dislocations, and finite-shaped crystals simulated using the Takagi–Taupin equations. Python implementations for each case are provided in a public GitHub repository, with the code structured for parallel computing.

Keywords: dynamical diffraction; Fourier optics; beam propagation method.

1. INTRODUCTION

Recently, we developed a new approach for solving time-dependent dynamic diffraction problems in distorted crystals using the Fast Fourier Transform Beam Propagation Method (FFT BPM). Our publication on this topic¹ focused on describing the theoretical approach and included several examples in the Bragg geometry. Here, we provide a more detailed description of the numerical implementation of our theory in Python. This implementation is optimized for parallel computing, and the Python code is available in a public GitHub repository.²

We will also present examples, including simulations of scattering from deformed crystals with arbitrary shapes in Bragg, Laue, and asymmetric geometries. The examples involving bent crystals and crystals with dislocations illustrate how to account for non-uniform strain distribution inside the crystal when simulating dynamic diffraction using the FFT BPM method. We benchmarked our code by successfully reproducing results from the literature for bent crystals, dislocations, and finite-shaped crystals simulated using the Takagi–Taupin equations.

For continuity, we will repeat some sections of our previous paper to maintain the reading flow.

2. THEORETICAL APPROACH

The scalar Helmholtz equation for a constant angular frequency ω :

$$(\nabla^2 + k(n(x, y, z))^2) E(x, y, z) = 0 \quad (1)$$

can be written in the following form:^{3,4}

$$\frac{d\psi}{d\hat{z}} = i \left(\sqrt{1 + \nabla_{\perp}^2 - \delta\epsilon(\hat{x}, \hat{y}, \hat{z})} - 1 \right) \psi \quad (2)$$

Further author information: (Send correspondence to J. Krzywinski)

J. Krzywinski.: E-mail: krzywins@gmail.com

A. Halavanau: E-mail: aliaksei@slac.stanford.edu

where $\hat{x}, \hat{y}, \hat{z} = kx, ky, kz$, k is the wave vector, ∇_{\perp}^2 is the Laplace operator taken with respect to the transverse coordinates $\hat{x}, \hat{y}, \delta\epsilon(\hat{x}, \hat{y}, \hat{z}) = n(\hat{x}, \hat{y}, \hat{z})^2 - \bar{n}^2$, $n(\hat{x}, \hat{y}, \hat{z})$ is the refractive index, \bar{n} is its average value and $E(x, y, z) = \psi(x, y, z)e^{-ikz}$. In the case of beams with narrow angular spectrum this equation can be approximated by:

$$\frac{d\psi}{d\hat{z}} = i \left(\sqrt{1 + \nabla_{\perp}^2} - \frac{\delta\epsilon(\hat{x}, \hat{y}, \hat{z})}{2\sqrt{1 - \langle k_x^2 + k_y^2 \rangle}} - 1 \right) \psi \quad (3)$$

Here the operator $\sqrt{1 + \nabla_{\perp}^2}$ in the denominator of the second term of the r.h.s was approximated by $\sqrt{1 - \langle k_x^2 + k_y^2 \rangle}$ where $\langle k_x^2 + k_y^2 \rangle$ is the average angular spectrum and $k_x^2 + k_y^2 = F[\nabla_{\perp}^2]$ is the Fourier transform of the ∇_{\perp}^2 operator. Eq. (3) leads to the following FFT BPM equation:

$$\psi(\hat{x}, \hat{y}, \hat{z} + \Delta\hat{z}) \approx F^{-1} \left\{ F[\psi(\hat{x}, \hat{y}, \hat{z})] e^{i\Delta\hat{z}\sqrt{1-k_x^2-k_y^2}} \right\} e^{i\Delta\hat{z}\frac{\delta\epsilon(\hat{x}, \hat{y}, \hat{z})}{2\cos\alpha}} \quad (4)$$

where F and F^{-1} denote Fourier and inverse Fourier transforms, $\cos\alpha = \sqrt{1 - \langle k_x^2 + k_y^2 \rangle}$. The angle α corresponds to the grazing incidence angle with respect to the propagation direction. We have previously applied Eq. (4) to take into account dynamic diffraction effects when simulating interaction of x-ray beams with gratings and multilayer optics.⁵⁻⁸

In a large class of dynamical diffraction problems, the angular spectrum of the scattered x-ray beams consists of two narrow bands centered around the incident and the reflection angles. The meaningful information is contained within these bands. One can remove the fast oscillating component related to inter-planar spacing from the physical picture and derive FFT BPM equations for slowly varying envelopes of transmitted and reflected beams. For simplicity, we are considering the 2D (x, z) case, and the generalization to the 3D case is straightforward. The procedure is outlined below. First, one can write the scattered x-ray field as a sum of two components:

$$\psi(\hat{z}, \hat{x}) = \psi(\hat{z}, \hat{x})_+ + \psi(\hat{z}, \hat{x})_- \quad (5)$$

Then the slowly varying envelopes are defined as follows:

$$\tilde{\psi}(\hat{z}, \hat{x})_+ = \psi(\hat{z}, \hat{x})_+ e^{-i\frac{k_d}{2}\hat{x}}, \quad \tilde{\psi}(\hat{z}, \hat{x})_- = \psi(\hat{z}, \hat{x})_- e^{i\frac{k_d}{2}\hat{x}} \quad (6)$$

where k_d is the reciprocal vector related to inter-planar spacing. Next we expand the exponential term related to dielectric susceptibility in Eq. (4) as:

$$e^{i\hat{z}\frac{\delta\epsilon(\hat{z}, \hat{x})}{2\cos\alpha}} = \sum_{n=-\infty}^{+\infty} \Delta\epsilon(\hat{z}, \hat{x})_n e^{ik_d n \hat{x}} \quad (7)$$

When crystal planes, taking part in the reflection, are perpendicular to the x -axis, one can describe the $\delta\epsilon(\hat{z}, \hat{x})$ in Eq. (7) as a complex harmonic function with the period equal to the inter-planar spacing:

$$\delta\epsilon(\hat{z}, \hat{x}) = \chi_0 + 2\chi_h \cos k_d \hat{x} \quad (8)$$

and $\chi_0 = \chi_{0r} + i\chi_{0h}$ and $\chi_h = |\chi_{rh}| - i|\chi_{ih}|$. The complex amplitude is composed of the χ_{0r} , χ_{0h} , χ_{rh} and χ_{ih} which could be found, for example, at the web page “x-ray dynamical diffraction data on the web” (<https://x-server.gmca.aps.anl.gov/x0h.html>) or XOP x-ray optics software toolkit.⁹

By applying the Jacobi–Anger expansion: $e^{iw\cos\theta} = \sum_{n=-\infty}^{\infty} i^n J_n(w) e^{in\theta}$ the first three expansion terms in Eq. (7) can be written in the following form:

$$\Delta\epsilon_0 = J_0 \left(z \frac{\chi_h}{\cos\alpha} \Pi(x, z) \right) e^{\frac{iz}{2\cos\alpha} \chi_0 \Pi(x, z)} \quad (9)$$

$$\Delta\epsilon_1 = \Delta\epsilon_{-1} = i J_1 \left(z \frac{\chi_h}{\cos\alpha} \Pi(x, z) \right) e^{\frac{iz}{2\cos\alpha} \chi_0 \Pi(x, z)} \quad (10)$$

where $\Pi(x, z) = 1$ inside the crystal, and $\Pi(x, z) = 0$ outside the crystal, with $J_n(w)$ being Bessel functions.

We treat deformation of the crystal as modification of the susceptibility:¹⁰

$$\Delta\epsilon'_n(\hat{z}, \hat{x}) = \Delta\epsilon_n(\hat{z}, \hat{x})e^{in\mathbf{k}_d\mathbf{u}(\hat{z}, \hat{x})} \quad (11)$$

where $\mathbf{k}_d\mathbf{u}$ is a scalar product of the reciprocal and displacement vectors. We note that \mathbf{k}_d is parallel to \hat{x} by definition, therefore only x -component of \mathbf{k}_d is used.

It has been shown in our previous paper¹ that one arrives at the following set of equations for slowly varying envelopes $\tilde{\psi}(\hat{z}, \hat{x})_+$ and $\tilde{\psi}(\hat{z}, \hat{x})_-$:

$$\begin{aligned} \tilde{\psi}(\hat{z} + \Delta\hat{z}, \hat{x})_+ &= \tilde{\psi}(\hat{z}, \hat{x})_{p+} \Delta\epsilon_0(\hat{z}, \hat{x}) + \tilde{\psi}(\hat{z}, \hat{x})_{p-} \Delta\epsilon'_{+1}(\hat{z}, \hat{x}) \\ \tilde{\psi}(\hat{z} + \Delta\hat{z}, \hat{x})_- &= \tilde{\psi}(\hat{z}, \hat{x})_{p-} \Delta\epsilon_0(\hat{z}, \hat{x}) + \tilde{\psi}(\hat{z}, \hat{x})_{p+} \Delta\epsilon'_{-1}(\hat{z}, \hat{x}), \end{aligned} \quad (12)$$

where $\tilde{\psi}(\hat{z}, \hat{x})_{p\pm} = F^{-1} \left[F \left[\tilde{\psi}(\hat{z}, \hat{x})_{\pm} \right] p_{\mp} \right]$. The operators $p_{\pm} = e^{i\Delta\hat{z}\sqrt{1-(k_x \pm \frac{k_d}{2})^2}}$ correspond to the Fourier image of ∇_{\perp}^2 which is shifted by $\pm \frac{k_d}{2}$ in the angular spectrum space. Equation (4) can be rewritten in the operator form as:

$$\begin{aligned} \psi(\hat{x}, \hat{y}, \hat{z} + \Delta\hat{z}) &\approx \prod_i A(a_i \Delta_z) B(b_i \Delta_z) \psi(\hat{x}, \hat{y}, \hat{z}), \\ A &= F^{-1} \left\{ F[\psi(\hat{x}, \hat{y}, \hat{z})] e^{ia_i \Delta\hat{z}\sqrt{1-k_x^2-k_y^2}} \right\}, \\ B &= e^{ib_i \Delta\hat{z} \frac{\delta\epsilon(\hat{x}, \hat{y}, \hat{z})}{2\cos\alpha}}. \end{aligned} \quad (13)$$

In the case of first order splitting, when $a_1 = 1, b_1 = 1$, Eq. (13) is reduced to Eq. (4). For most of the practical problems this splitting scheme is accurate. Higher order splitting improves the efficiency of the FFT BPM for large Bragg angles. For instance, when $a_1 = 0.0, a_2 = 1.0, b_1 = 0.5, b_2 = 0.5$, Eq. (13) is accurate up to $O(\Delta z^2)$, and when $t = 1.3512, a_1 = 0.0, a_2 = t, a_3 = 1 - 2t, a_4 = t, b_1 = t/2, b_2 = (1-t)/2, b_3 = (1-t)/2, b_4 = t/2$ it is accurate up to $O(\Delta z^4)$; see.¹¹

We point out that Eqs. (12) can be treated as a two-beam approximation for the FFT BPM. These equations are analogous to the Takagi-Taupin equations (TTE) in two-beam approximation.¹⁰ However, there is a significant difference between TTE and FFT BPM equations. The TTE equations are a system of hyperbolic equations where the second derivatives in the transverse direction with respect to beam propagation are neglected. Therefore, diffraction of the x-rays is not taken into account in the TTE formulation. The numerical algorithms for solving TTE, which are presented in the literature, typically require setting the boundary conditions. This could be a difficult problem itself in complicated geometries or when the boundaries are not very well defined. On the other hand, the FFT BPM equations are a system of parabolic equations that automatically includes diffraction. Also, as we have mentioned before, the FFT BPM method is especially convenient when dealing with complicated shapes or non-homogeneous boundaries.

3. NUMERICAL IMPLEMENTATION

The algorithm is embedded in a class; the user provides configuration file (in yaml format) to run a simulation instance, for example for a given angle of incidence and/or wavelength. Since most of the diffraction problems are "linear", all instances, in principle, can be evaluated in parallel. The input configuration file provides the main input simulation parameters and data: photon energy, crystallographic data, electric susceptibilities, crystal geometry, numerical grid parameters, integration methods and parameters, x-ray beam properties, crystal deformation data and program settings.

The crystal boundaries can be defined directly in the configuration file for simple cases, such as those in Bragg geometry, or by generating a mask with additional Jupyter notebooks and saving it to a file. We have

provided examples of the latter approach for simulations of asymmetric reflections and scattering from 3D finite crystals with cuboid, cubic, and hemispherical shapes.

The user interacts with the code using jupyter notebooks or user scripts (similar to SRW approach). Python scripts are grouped in three classes:² XBPM, XCRYSTAL and XCRTOOLS

The main propagation equations, Eqs. (9-14) from our previous paper,¹ are encoded in the XBPM class. The XCRTOOLS class is used to configure the incident x-ray beam and to provide numerical tools needed for manipulations such as FFT, padding, cropping, interpolation, etc. The XCRYSTAL class incorporates the parameters and data provided in the yaml configuration file and creates the main 'run3D()' function. The 'run3D()' can be used to define a single realization reflection object that is computed in parallel to other reflections having different parameters e.g. photon energy, incidence angle, etc. Thus, the calculation of rocking curves or time-dependent diffraction can be implemented as an embarrassingly parallel problem.

4. SIMULATION OF REFLECTION IN THE LAUE GEOMETRY AND ASYMMETRIC REFLECTIONS

Previously we have shown simulations of the symmetric Bragg reflection cases. Now let us consider the Laue geometry and the diamond crystal for (400) reflection at 9.831 keV photon energy. The crystal has a form of a slab. Let us define the *s*-axis to be perpendicular to the crystal's surfaces. The orientation of the *s*-axis with respect to the crystallographic planes is defined by the *asymm_angle* parameter in the configuration yaml file. The Bragg geometry corresponds to *asymm_angle* = 0 deg and the Laue geometry corresponds to the *asymm_angle* = 90 deg.

An example of a simulation of reflection in the Laue geometry is implemented in a Jupyter notebook, which can be found in the `example` subdirectory of the Crystal-fft-bpm GitHub repository.² The corresponding configuration file is located in the `config` subdirectory. The results of the simulation are presented in Fig. 1. Two cases are simulated: when the incident beam is at the Bragg angle (top left) and at the Bragg angle + 1.5 μ rad (top right).

The names of the Jupyter notebook and the configuration files are:

- `SingleRealization_C400_Laue.ipynb`
- `C400_9p8keV_LaueFig1.yaml`

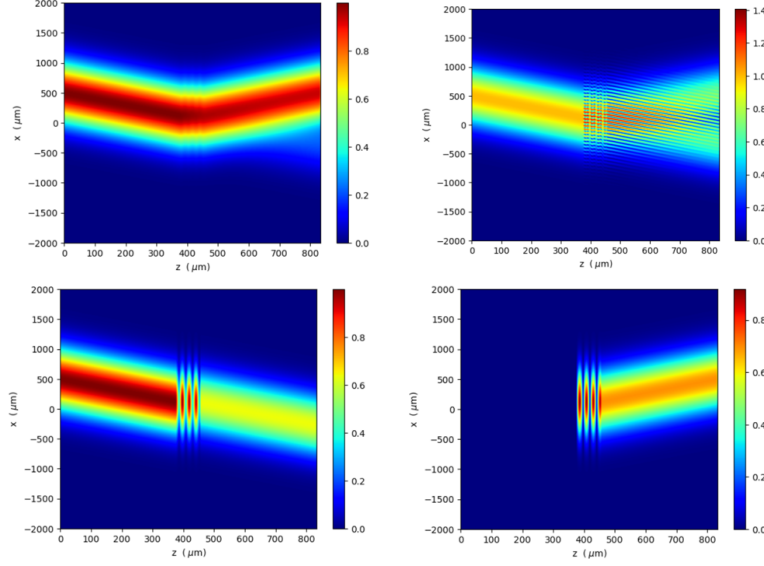


Figure 1. 2D visualization of a diamond (400) Laue reflection, with the incident beam at the Bragg angle (top left) and at the Bragg angle $+ 1.5 \mu\text{rad}$ (top right). The bottom row shows the intensity of the transmitted component $\tilde{\psi}_+$ (left) and the reflected part $\tilde{\psi}_-$ for the $1.5 \mu\text{rad}$ deviation from the Bragg angle. The Pendellösung oscillations are clearly visible. The color scale units are arbitrary.

Asymmetric reflection geometries occur when $0^\circ < \text{asymm_angle} < 90^\circ$. A visualization of asymmetric reflection for asymmetry angles of $\text{asymm_angle} = 15^\circ$ and -15° is shown in Fig. 2. The deviations from the Bragg condition for these angles were $20 \mu\text{rad}$ and $10 \mu\text{rad}$, respectively. The corresponding Jupyter notebooks for generating the crystal boundary mask, performing the beam propagation, and the configuration file for $\text{asymm_angle} = 15^\circ$ are:

- `geometry-AsymmetricReflection15deg.ipynb`
- `SingleRealization_C400_AsymmetricReflection.ipynb`
- `C400_9p8keV_LaueAssymRefl15degFig2.yaml`

To run the simulation, the crystal boundary mask file must first be generated by executing the `geometry-AsymmetricReflection15deg.ipynb` notebook.

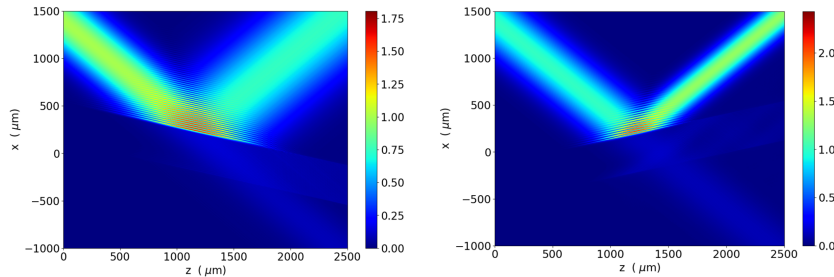


Figure 2. 2D visualization of field amplitudes for a diamond (400) asymmetric reflection, $\text{asymm_angle}=15 \text{ deg}$ (left), $\text{asymm_angle}=15 \text{ deg}$ (right). Color scale units are arbitrary.

The rocking curve for the Laue case was computed using the parallel algorithm outlined in the previous paragraph, with parallelization performed with respect to the incident angle. The results obtained using the FFT BPM method are compared to those of the XOP toolkit,⁹ as shown in Fig. 3. We note excellent agreement between our method and the XOP output. The very small differences between the two plots can be attributed to the finite beam waist and numerical errors due to the finite mesh size. The corresponding Python code for parallel computing, the Jupyter notebook for displaying the results, and the configuration file are:

- `run_parallel_angleC400_9831eV_Laue.py`
- `process-parallel-data-angleC400_9p8keV_Laue.ipynb`
- `C400_9p8keV_LaueFig3.yaml`.

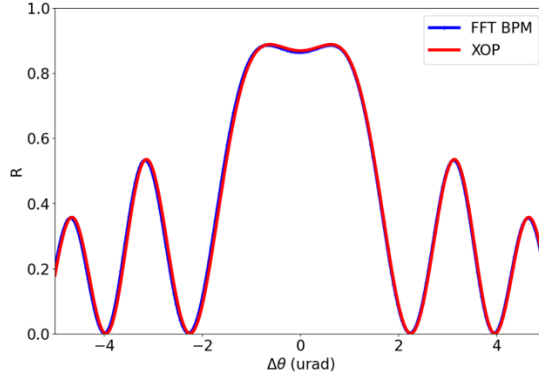


Figure 3. Rocking curve simulated in the Laue geometry for a $82 \mu\text{m}$ thick diamond crystal at 9.813 keV photon energy.

5. SIMULATIONS OF BEND CRYSTALS

Bend crystals have been successfully used to build single-shot spectrometers for XFEL applications.^{12,13} To benchmark our code, we simulated rocking curves for a bend diamond crystal applied at the European X-ray Free-Electron Laser. The rocking curves of this crystal were theoretically investigated in the article by Samoylova et al.¹⁴ In that paper the simulations were done for a $20 \mu\text{m}$ thick crystal bent around the axis [001] (y axis) with a surface orientation [110] (x axis). The displacement u_x for the cylindrically bent crystal can be expressed as:

$$u_x = \frac{1}{2R} (z^2 + \nu x^2) \quad (14)$$

where R is the bending radius and ν is the Poisson ratio.¹⁴ The scattering from the bend crystal was derived by a numerical solution of the Takagi–Taupin equations based on the algorithm proposed by Authier et al.¹⁰ The authors considered a symmetric Bragg reflection 440 of monochromatic x-ray at 14.4 keV. The incident wave front was restricted to a width of $10 \mu\text{m}$ by an entrance slits.

We have simulated the same case using our FFTBPM method. The rocking curves for two bending radii of $R = 65 \text{ mm}$ and $R = 95 \text{ mm}$ are presented in Fig. 4

The results calculated using our FFT BPM method, presented in Fig. 4, are identical to the numerical solution of the Takagi–Taupin equations shown in Fig. 2 in the article by L. Samoylova et al.¹⁴ The corresponding Python code for parallel computing, the Jupyter notebook for displaying the results, and the configuration files for $R = 65 \text{ mm}$ and $R = 95 \text{ mm}$ are:

- `run_parallel_angleC440CurvedSpectrometerR65.py`

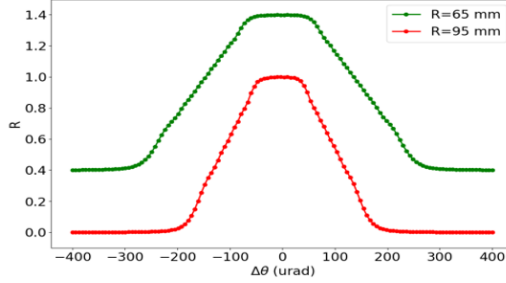


Figure 4. Rocking curves simulated for bending radii of 65 and 95 mm.

- `run_parallel_angleC440CurvedSpectrometerR95.py`
- `process-parallel-data-angleC440Spectrometer.ipynb`
- `CrystalC440Fig4_R65.yaml`
- `CrystalC440Fig4_R95.yaml`

In order to run the notebook and display the results, one needs to run the Python code twice using either of the configuration files.

6. SIMULATIONS OF DISLOCATIONS

Our FFT BPM method can be easily applied to simulate crystal defects such as dislocations. We will simulate two cases that were investigated using the TTE approach: a Laue [220] and [440] reflections from a Si crystal in the presence of screw and mixed dislocations.^{10 15 16}

The first case follows an example presented in the work of Besedin et al.¹⁵ A plane-parallel silicon plate was chosen as the model crystal. In this structure, undissociated straight line dislocations have Burgers vectors with magnitude $|\mathbf{b}| = a/\sqrt{2}$, where a is the lattice constant. The Burgers vectors and the diffraction vector \mathbf{h} are directed along the (110) axis.

We will consider two types of dislocations here: a screw dislocation and a mixed 60-degree dislocation. The screw dislocation has the unit dislocation line vector $\boldsymbol{\tau}$ parallel to the Burgers vector (along the (110) axis). The mixed 60-degree dislocation has the unit dislocation line vector $\boldsymbol{\tau}$ parallel to the (101) axis, as shown in Fig. 5.

According to¹⁵ the displacement vector $\mathbf{u}(\mathbf{r})$ for a straight-line dislocation in its intrinsic coordinate system (x_0, y_0, z_0) , has the form:

$$\mathbf{u} = \frac{\mathbf{b}}{2\pi} \arctan \frac{z_0}{y_0} + \frac{\mathbf{b} - \boldsymbol{\tau}(\mathbf{b} \cdot \boldsymbol{\tau})}{2\pi} \frac{y_0 z_0}{2(1-\nu)(y_0^2 + z_0^2)} - \frac{\boldsymbol{\tau} \times \mathbf{b}}{2\pi} \left(\frac{1-2\nu}{4(1-\nu)} \ln(y_0^2 + z_0^2) + \frac{y_0^2 - z_0^2}{4(1-\nu)(y_0^2 + z_0^2)} \right) \quad (15)$$

where the x_0 axis is directed along $\boldsymbol{\tau}$, the z_0 axis is directed along the vector $\boldsymbol{\tau} \times \mathbf{b}$, and ν is the Poisson ratio ($\nu = 0.22$ for silicon).

We are only concerned with the u_x component of the \mathbf{u} vector. Therefore, for the case considered here the equation (10) simplifies to:

$$u_x = \frac{a}{\sqrt{2}2\pi} \arctan \frac{z_0}{y_0} \quad (16)$$

for the screw dislocation and to

$$u_x = \frac{a}{\sqrt{2}2\pi} \left(\arctan \frac{z_0}{y_0} + \frac{y_0 z_0}{4(1-\nu)(y_0^2 + z_0^2)} \right) \quad (17)$$

for the 60 degree mixed dislocation. The coordinates (x_0, y_0, z_0) are related to the coordinates (x, y, z) via the matrix transformation \mathbf{M} , where x_d , y_d and z_d are positions of origin of the intrinsic coordinate system of dislocation with respect to the origin of the coordinates (x, y, z) .

$$\begin{bmatrix} x_0 \\ y_0 \\ z_0 \end{bmatrix} = \mathbf{M} \begin{bmatrix} x - x_d \\ y - y_d \\ z - z_d \end{bmatrix} \quad (18)$$

where $\mathbf{M} = \begin{bmatrix} 1 & 0 & 0 \\ 0 & -1 & 0 \\ 0 & 0 & 1 \end{bmatrix}$ for the screw dislocation case, and $\mathbf{M} = \begin{bmatrix} \frac{1}{2} & -\frac{\sqrt{3}}{2} & 0 \\ \frac{\sqrt{3}}{2} & -\frac{1}{2} & 0 \\ 0 & 0 & 1 \end{bmatrix}$ for the mixed 60 degrees dislocation case.

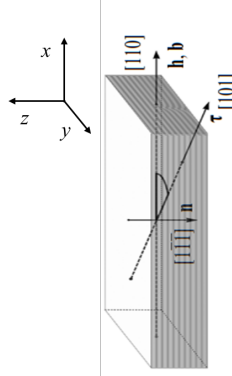


Figure 5. Geometry of the Laue [220] reflection from a Si crystal in the presence of screw and mixed dislocations. The screw dislocation has the unit dislocation line vector τ parallel to the Burgers vector (along the (110) axis). The mixed 60 degrees dislocation has the unit dislocation line vector τ parallel to the (101) axis. The pattern on the crystal sides indicates the Pendellösung fringes.

Results of XBPM simulations are presented in Fig. 6 and Fig. 7. In general, the XBPM results match those obtained by the TTE method by Besedin et al.¹⁵ For example, the intensity distribution inside the crystal, shown on the left side of Fig. 6, coincides with the intensity presented in Fig. 4(a) of¹⁵. Similarly, the distribution shown on the left side of Fig. 7 agrees with the intensity pattern presented in Fig. 4(e) of¹⁵. We also noticed, when comparing the results, that the vertical scale of Fig. 4(e) in the work of I. S. Besedin et al. was not consistent with the trigonal coordinate system used, requiring an increase in scale of approximately 25 %. Only after making this correction did the results obtained by XBPM and TTE agree.

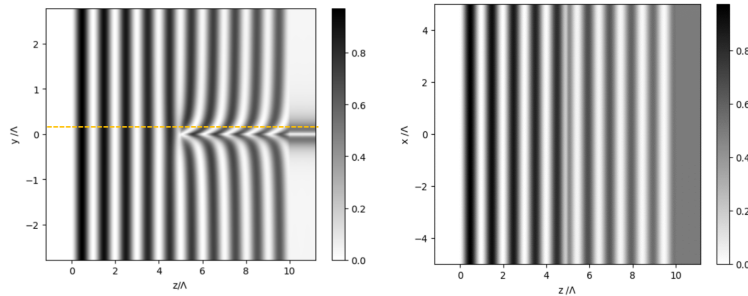


Figure 6. The intensity of the reflected wave in the Si crystal with a screw dislocation, calculated using the XBPM method, is shown in the yz (left) and xz (right) planes. The cross-section in the xy plane is taken at the position of x, indicated by the dotted line in the left figure.

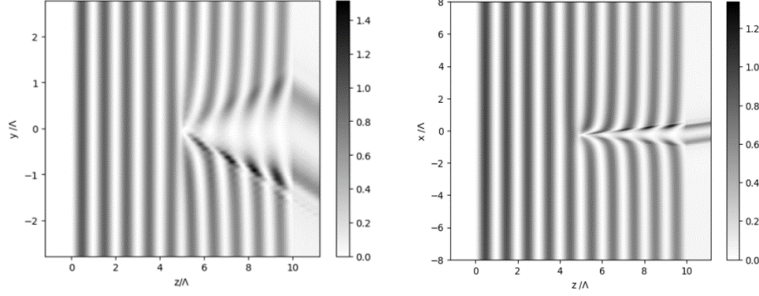


Figure 7. Intensity of the reflected wave in the Si crystal with a mixed 60 degrees dislocation. The results are identical to the results obtained by the TTE method (Fig. 4(e) in ¹⁵).

We also show in Fig. 8 the intensity of the diffracted wave in the xy plane after the beam leaves the crystal. This corresponds to X-ray topography images taken with a monochromatic beam (Fig. 8). The corresponding Jupyter notebooks and configuration files are:

- `SingleRealization_Si220_17p45keVSCREWDislChukhovskii.ipynb`
- `Si220_17p45keVSCREWDislChukhovskii.yaml`

for the screw dislocation and

- `SingleRealization_60degDislocationSi220_17p45keVChukhovskii.ipynb`
- `Si220_17p45keV60degDislChukhovskii.yaml`

for the 60-degree mixed dislocation.

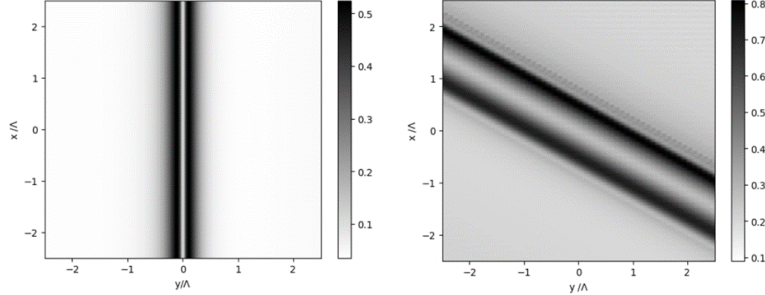


Figure 8. Intensity of the diffracted wave in the xy plane after the beam exits the crystal, left for the screw dislocation and, right for the mixed 60 degrees dislocation.

In the previous examples, the dislocation lines were parallel to the crystal's scattering surface. Now, we will present an example where the dislocation line is not parallel to the surface. We will simulate an X-ray section topography experiment as described in the paper by G. Kowalski et al. ¹⁶ The simulations were performed for the (440) and (220) reflection at 17,450 eV photon energy. A 415 μm thick [112]-oriented silicon single crystal contained a mixed 60 degrees [110] dislocation line with a $1/2$ [1 -1 0] Burgers vector \mathbf{b} . The geometry of the

simulation is shown in Fig. 9. The transformation matrix \mathbf{M} for this case is given by : $\mathbf{M} = \begin{bmatrix} 0 & -\sqrt{\frac{2}{3}} & -\sqrt{\frac{1}{3}} \\ 1 & 0 & 0 \\ 0 & \sqrt{\frac{1}{3}} & -\sqrt{\frac{2}{3}} \end{bmatrix}$.

In the X-ray section topography method, the incoming X-ray beam is shaped by a slit with a width on the order of micrometers. In our case we have applied 5 μm wide slit.

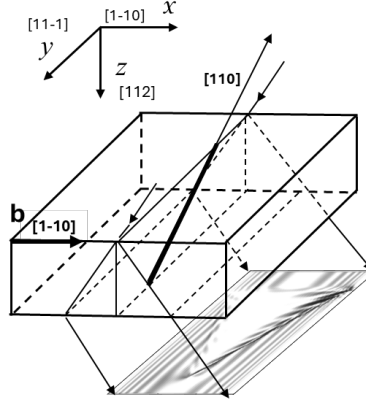


Figure 9. The geometry of the simulation.

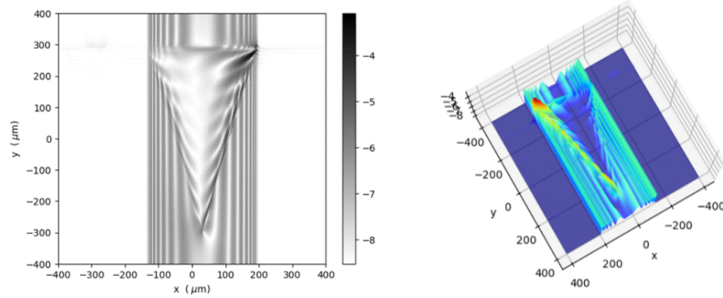


Figure 10. Simulation of a topography of a mixed 60 deg dislocation in a Si crystal by the Lang method for (440) reflection. The intensity scale is logarithmic

The results of the simulations, presented in Fig. 10 and Fig. 11, are in qualitative agreement with those presented in the work of G. Kowalski et al.¹⁶ Unfortunately, we were unable to make a quantitative comparison, as the authors of the cited work did not provide sufficient information regarding intensity scaling in the presented figures.

The corresponding Jupyter notebooks and configuration files are:

- `SingleRealization_Si440_60deg_DislocationGronkowski.ipynb`
- `Si440_17p45keVDislk60degGronkowski.yaml`

for the (400) reflection,

and

- `SingleRealization_Si220_60deg_DislocationGronkowski.ipynb` and
- `Si220_17p45keVDislk60degGronkowski.yaml`

for the (200) reflection.

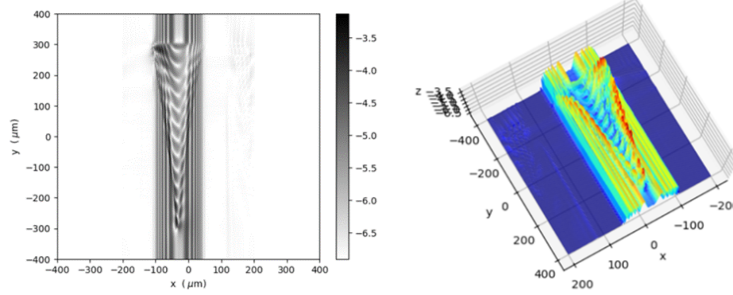


Figure 11. Simulation of a topography of a 60 deg dislocation in a Si crystal by the Lang method for (220) reflection. The intensity scale is logarithmic.

7. CRYSTALS WITH ARBITRARY SHAPES AND STRAIN DISTRIBUTIONS

Our FFT BPM method simplifies simulations compared to the TTE method by eliminating the need to solve boundary condition problems. Therefore, it is well-suited for simulating scattering from finite crystals with arbitrary shapes and strain distributions. All that is required are maps of the crystal boundaries and the deformation vector component u_x , which is perpendicular to the crystal planes.

We will illustrate this approach with several examples presented below.

First, we apply our method to simulate reflection from a Si(004) rectangular crystal with dimensions $100 \mu\text{m} \times 300 \mu\text{m}$ at 12 keV photon energy, an example also simulated in the article “*X-ray dynamical diffraction from single crystals with arbitrary shape and strain field: A universal approach to modeling*”.¹⁷ The crystal boundary map is generated using the `geometry-finite Si crystal-2D.ipynb` Jupyter notebook.

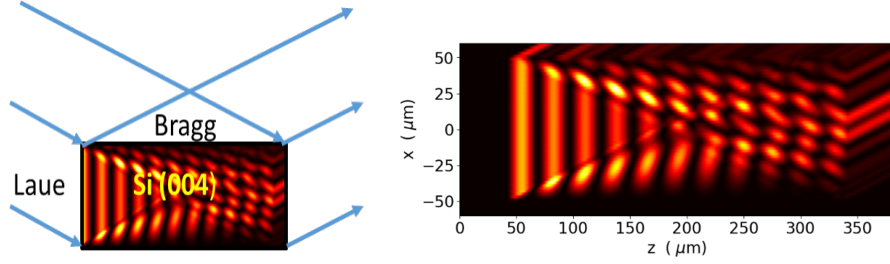


Figure 12. Reflection from a Si(004) rectangular crystal with dimensions $100 \mu\text{m} \times 300 \mu\text{m}$ at 12 keV photon energy. Pendellösung fringes are visible at the crystal’s entrance. A more complicated diffraction pattern develops for the mixed Laue - Bragg case.

The result of the simulation, which is identical to the one presented in,¹⁷ is shown in Fig. 12. Pendellösung fringes are visible at the crystal’s entrance. A more complicated diffraction pattern develops for the mixed Laue - Bragg case. The corresponding Jupyter notebooks and configuration files are:

- `SingleRealization_Si400_12keV_FiniteCrystal-2D.ipynb`
- `Si400_12keV_finite_Crystal_2D.yaml`

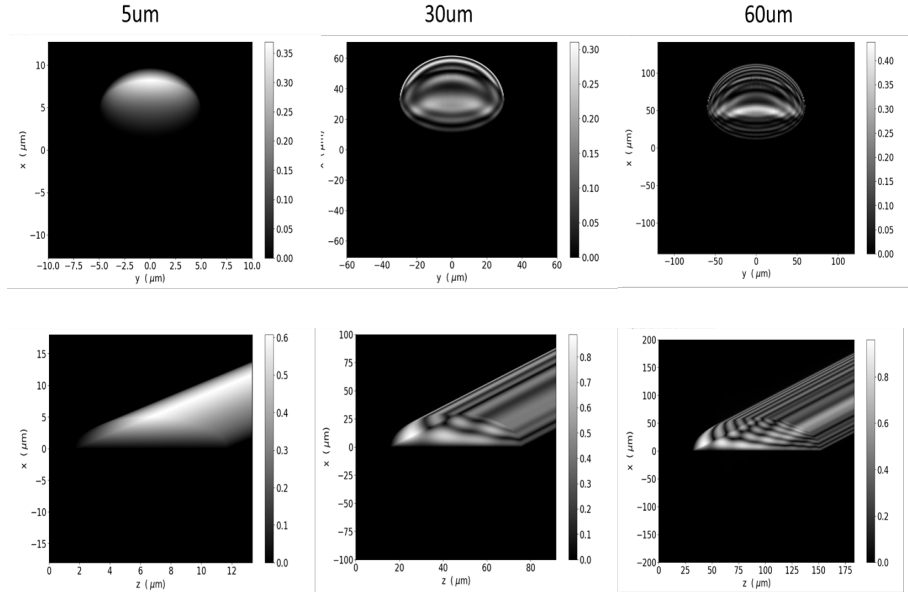


Figure 13. Reflection from a C(400) semisphere crystals with dimensions 5 μm , 30 μm and 60 μm at 9.8 keV photon energy. Cross-section of the reflected wave in the xz -plane at $y=0$ (lower row) and reflected wave intensity in the xy -plane after exiting the crystal. A complicated diffraction pattern develops when the crystal size is larger than extinction length.

Next, we present simulation results for semi-spherical C(400) crystals with radii of 5 μm , 30 μm , and 60 μm at 9.8 keV photon energy, shown in Fig. 13. These results highlight the necessity of accounting for dynamical diffraction effects as the crystal size approaches or exceeds the extinction length. For a radius of 5 μm , the simulated intensity closely resembles predictions from kinematic theory. However, for larger radii, the reflected wave intensity exhibits a complex pattern due to dynamical effects.

The Jupyter notebooks for running the simulation, generating the crystal boundary map, and the configuration file for a radius of 10 μm are:

- `SingleRealization_C400-hemi-sphere.ipynb`
- `geometry-hemi-sphere.ipynb`
- `C400_9p8keV_Laue-hemi-sphere.yaml`

Additionally, we provide a Python script for simulating an angular scan of the hemisphere with a 10 μm radius as it is rocked in the xz -plane. Far-field images simulated 2 m from the crystal over an angular range of $\pm 10 \mu\text{rad}$ are shown in Fig. 14. For reference, Fig. 15 displays the corresponding near-field images.

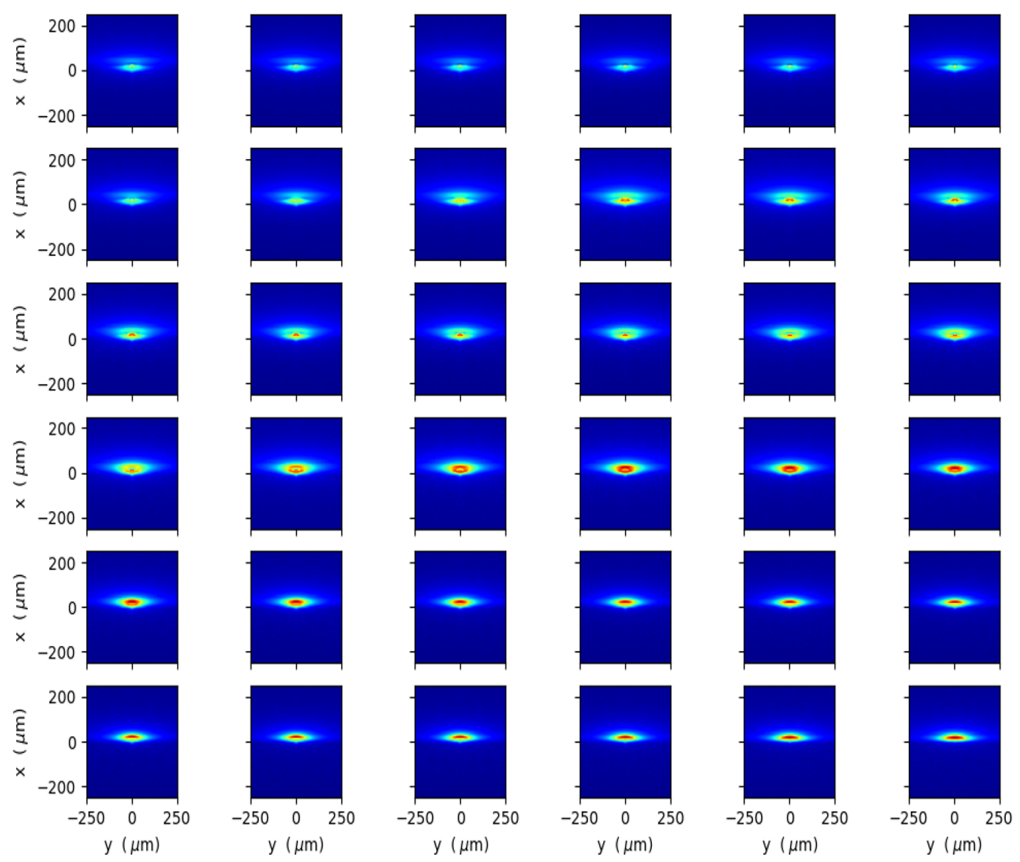


Figure 14. Far-field images simulated 2 m from the crystal, obtained from an angular scan of $\pm 10 \mu\text{rad}$.

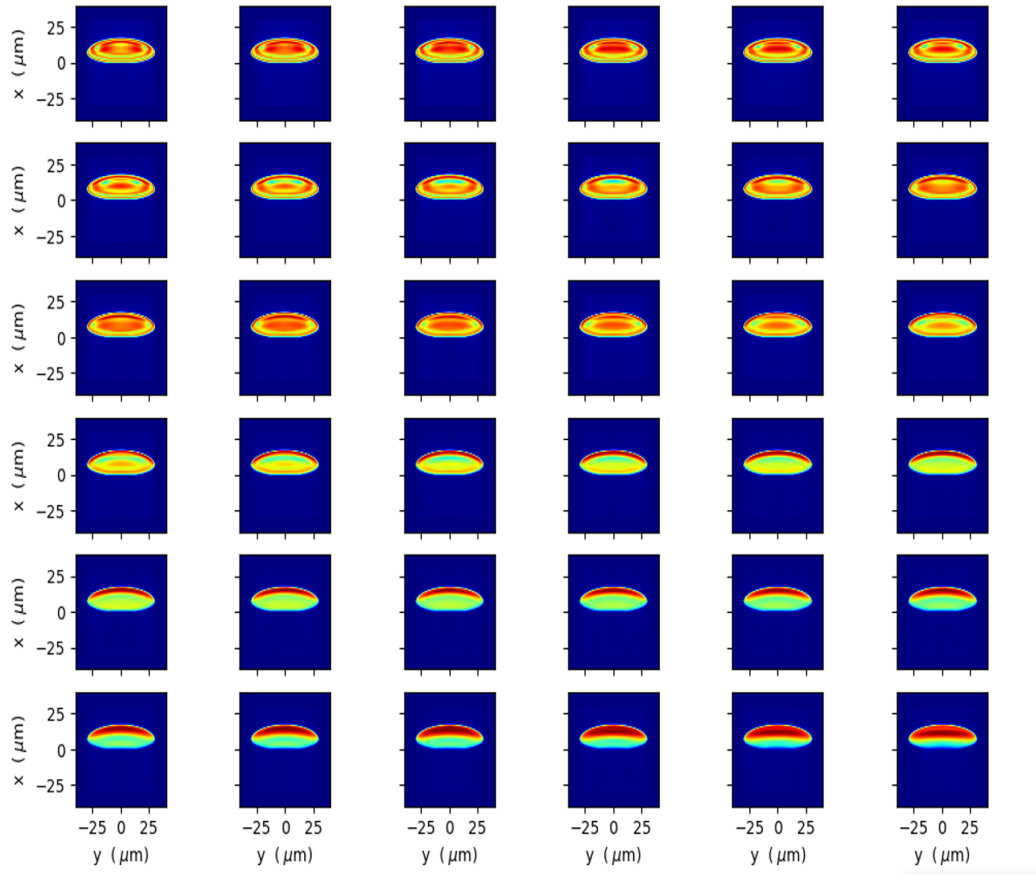


Figure 15. Near-field images obtained from an angular scan of $\pm 10 \mu\text{rad}$.

The corresponding Python code for parallel computing, the configuration file, and the Jupyter notebook for displaying the results are as follows:

- `run_parallel_angleC400_9p8keV_Laue_Asym-sphere.py`
- `C400_9p8keV_Laue_Asym-sphere-par.yaml`
- `process-parallel-data-angleC400_9p8keV_Laue_Asym-sphere.ipynb`

In the final example in this section, we simulate Si(440) reflection from a $10 \mu\text{m}$ silicon cube crystal deformed by a mixed 60° [110] dislocation with a $\frac{1}{2}[1 -1 0]$ Burgers vector at a photon energy of 17,450 eV. The simulation results are shown in Fig. 16 and Fig. 17. We highlight the numerical efficiency of our approach: the simulations, performed on a $300 \times 200 \times 300$ rectangular grid, ran on a single node of the Perlmutter high-performance machine¹⁸ and took approximately 13 seconds.

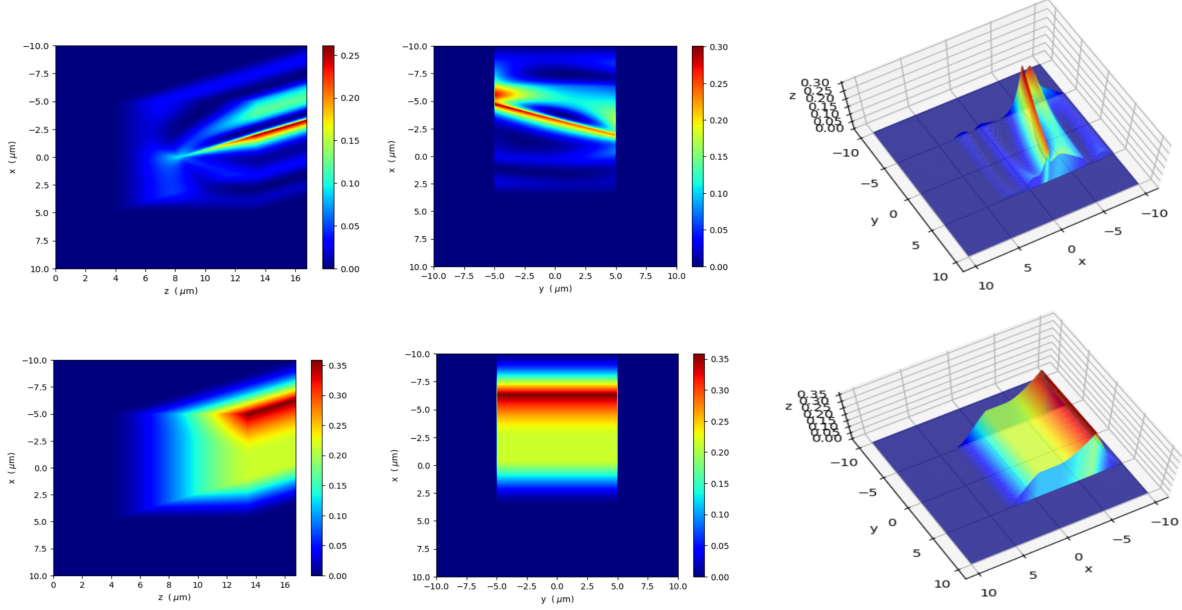


Figure 16. Si(440) reflection from a $10 \mu\text{m}$ silicon cube crystal at a photon energy of 17,450 eV. The crystal is deformed by a mixed $60^\circ [110]$ dislocation with a $\frac{1}{2}[1\bar{1}0]$ Burgers vector. The top left panel shows the cross-section of the reflected wave in the xz -plane at $y = 0$, while the top center and right panels display the reflected wave intensity in the xy -plane after exiting the crystal. For comparison, the lower row presents simulation results for the same crystal without a dislocation.

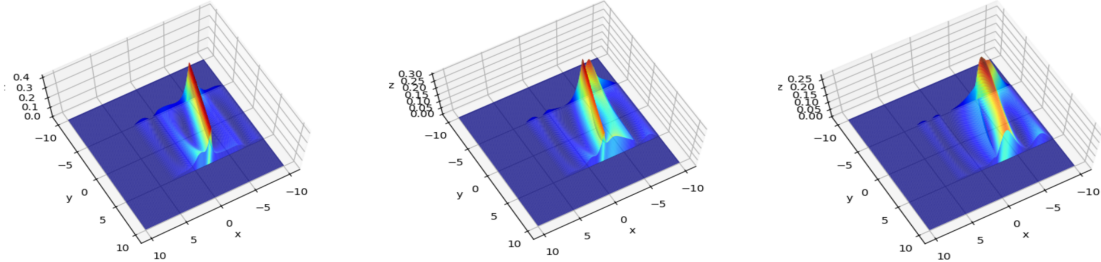


Figure 17. Reflected wave intensity in the xy -plane after exiting the crystal for different incidence angles: at the Bragg angle (center), $-3 \mu\text{rad}$ below the Bragg angle (left), and $+3 \mu\text{rad}$ above the Bragg angle (right).

The Jupyter notebooks for running the simulation, generating the crystal boundary map, and the configuration file for a $10 \mu\text{m}$ silicon cube crystal deformed by a mixed $60^\circ [110]$ dislocation are:

- `SingleRealizationFiniteCrystal_Si440_60deg_Dislocation.ipynb`
- `geometry-finite Si440crystal-60degDislocation.ipynb`
- `Si440_17p45keVDislk60degGronkowskiFiniteCrystal3D.yaml`

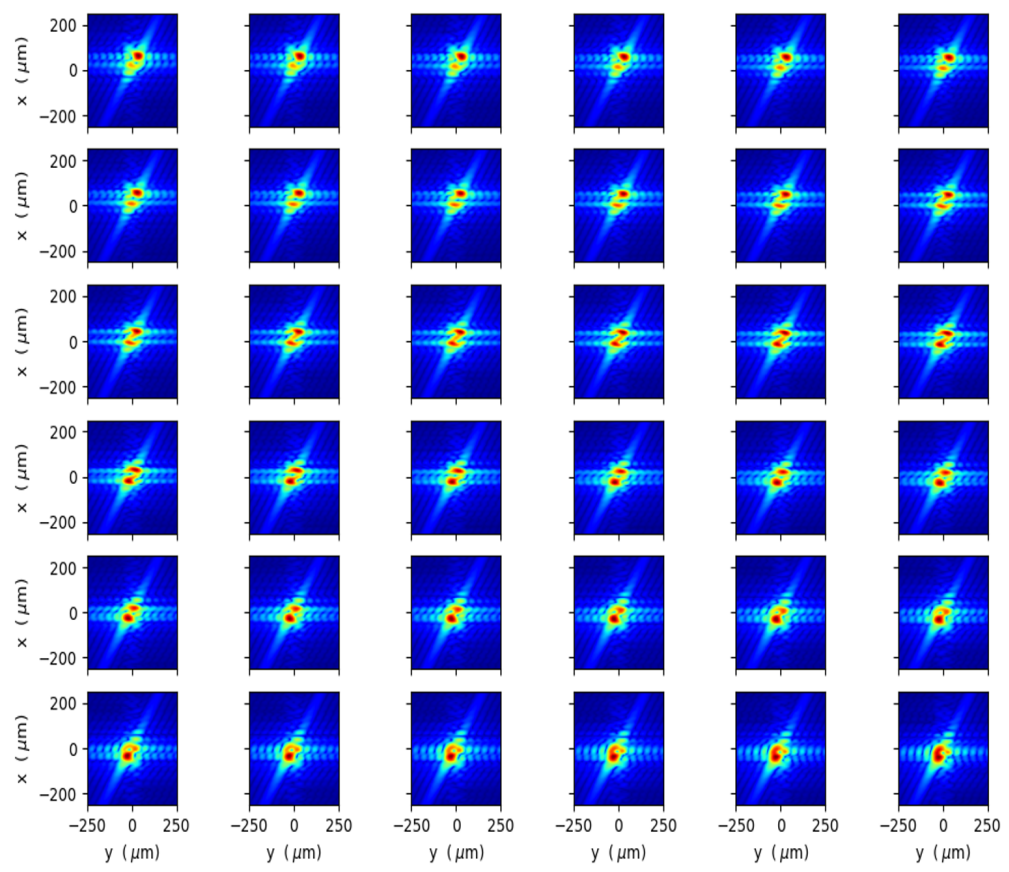


Figure 18. Far-field images simulated 4 m from the crystal, obtained from an angular scan of $\pm 10 \mu\text{rad}$.

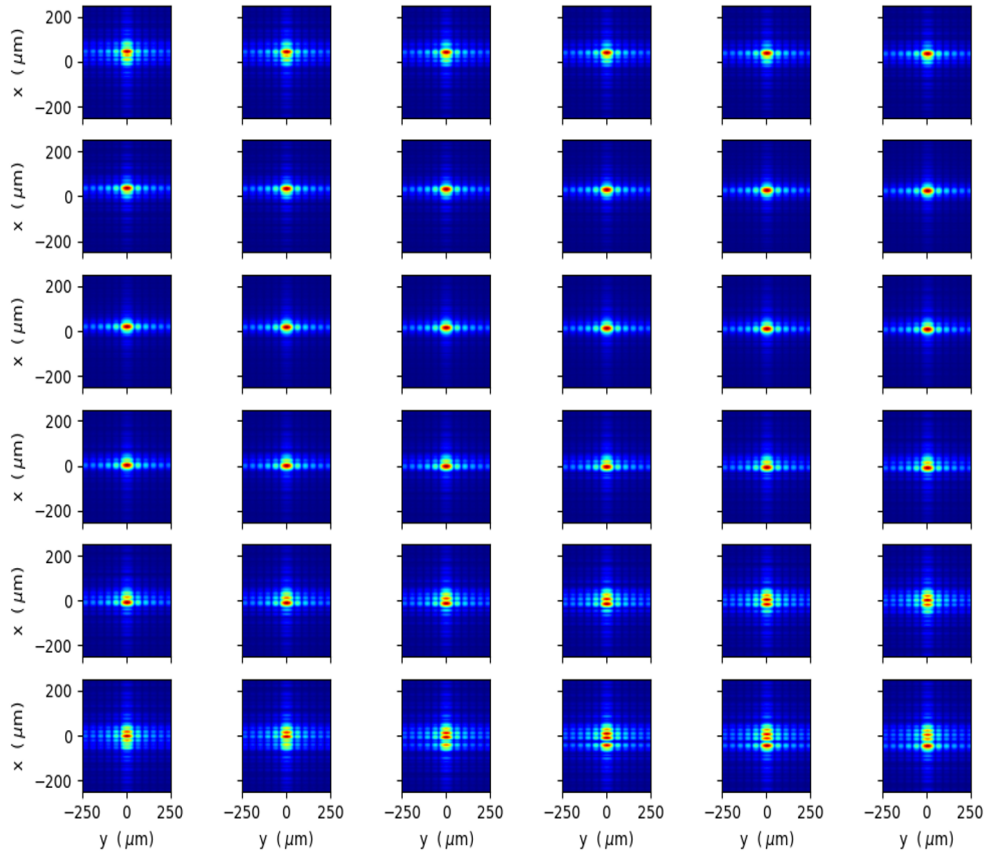


Figure 19. Far-field images simulated 4 m from the crystal without dislocation, obtained from an angular scan of $\pm 10 \mu\text{rad}$.

We also provide a Python script that simulates an angular scan as the crystal is rocked in the xz -plane. Far-field images simulated 4 m from the crystal over an angular range of $\pm 10 \mu\text{rad}$ are shown in Fig. 18. For comparison, Fig. 19 presents similar images simulated for the same crystal without the dislocation.

The corresponding Python code for parallel computing, the configuration file and the Jupyter notebook for displaying the results are as follows:

- `run_parallel_angle_scanFiniteCrystal_Si440_60deg_Dislocation.py`
- `Si440_17p45keVDislk60degGronkowskiFiniteCrystal3Dpar.yaml`
- `process-parallel-data-angleFiniteCrystal_Si440_60deg_Dislocation.ipynb`

We note that FFT BPM simulations can be particularly useful in the analysis of Bragg coherent X-ray diffractive imaging (CXDI) data, especially when the crystal size approaches the extinction length. Because of the simplicity and computational efficiency of the FFT BPM method, it could be integrated into iterative algorithms to retrieve the shape and strain distribution of the investigated crystal.

8. TIME-DEPENDENT SIMULATION OF REFLECTION FROM DISTORTED CRYSTALS

The following section provides an overview of the Jupyter notebooks, configuration files, and Python scripts available in the public repository that were used for the time-dependent simulations described in Ref.¹ The theoretical background and detailed simulation conditions are presented in that reference. Each example in the repository corresponds directly to the figures in Ref.,¹ allowing users to reproduce and extend the published results.

8.1 Benchmarking of the TD FFT BPM Method

The first set of examples benchmarks the time-dependent Fast Fourier Transform Beam Propagation Method (TD FFT BPM) against the analytical solution for perfect crystals presented by Shvyd'ko and Lindberg.¹⁹ The left and right panels in Fig. 20 correspond to Figs. 5 and 6 in Ref.,¹ respectively; note that in the caption of Fig. 5 in Ref.,¹ the beam waist W_0 was mistakenly listed as $50\text{ }\mu\text{m}$, whereas the correct value is $250\text{ }\mu\text{m}$.

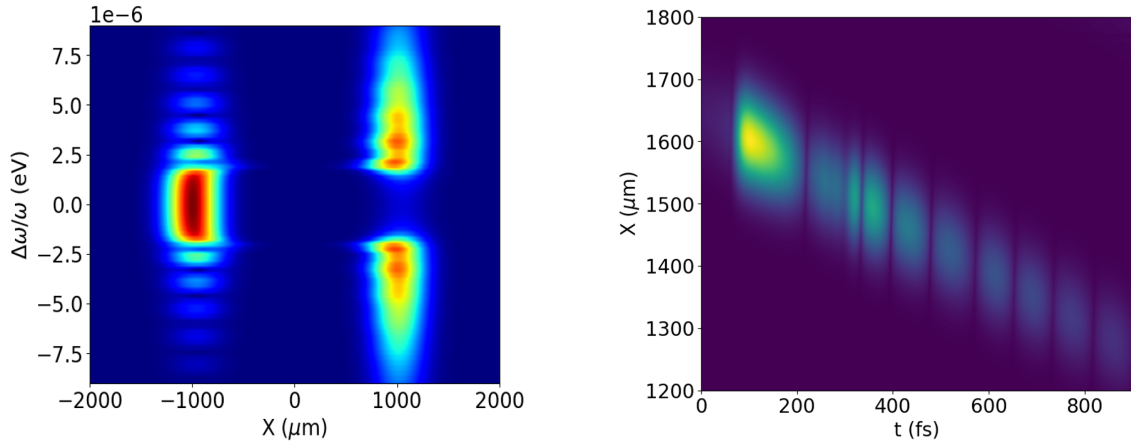


Figure 20. Spatio-spectral intensity profiles of the reflected and transmitted beams for a $50\text{-}\mu\text{m}$ -thick $\text{C}^*(333)$ diamond crystal at $y = 0$ using an incident Gaussian beam with $t = 10\text{ fs}$, $W_0 = 250\text{ }\mu\text{m}$, and $\omega_0 = 12.8\text{ keV}$ (left), and spatio-temporal intensity profiles of the Bragg-diffracted beam computed with $W_0 = 50\text{ }\mu\text{m}$ while keeping all other parameters the same (right); color-scale units are arbitrary.

The simulations shown in Fig. 20 were produced using the following Python scripts, configuration files, and Jupyter notebooks:

Left panel:

- `run_parallel-omegaC333-250um.py`
- `C333_Omega12p8keV_waist250um.yaml`
- `process-parallel-data-omegaC333-250.ipynb`

Right panel:

- `run_parallel-omegaC333-50um.py`
- `C333_Omega12p8keV_waist50um.yaml`
- `process-parallel-data-omegaC333-50.ipynb`

As noted in Ref.,¹ the FFT-BPM method shows perfect agreement with the theoretical calculations of Shvyd'ko and Lindberg (2012).

8.2 Reflection from a Deformed Crystal

The second set of examples demonstrates time-dependent reflection from a deformed crystal. These simulations correspond to Figs. 7, 8 and 10 in Ref.¹ The examples show how to include deformation fields within the FFT-BPM framework to model the resulting time-dependent diffraction response.

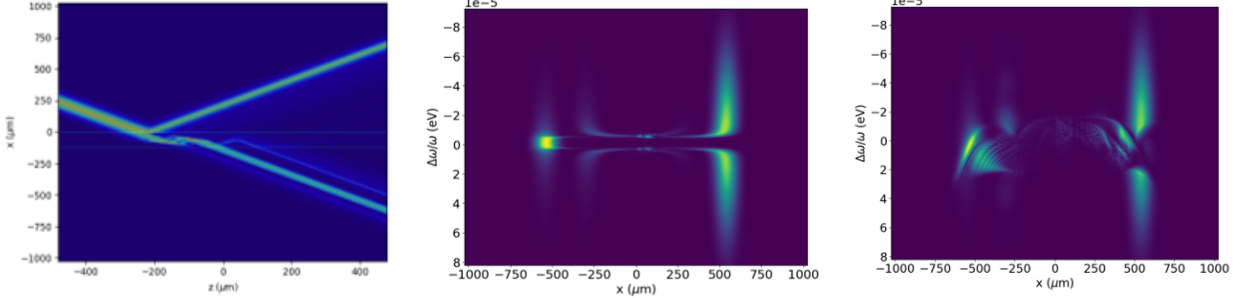


Figure 21. 2D visualization of Bragg reflection from the deformed crystal at the central XFEL frequency (left), and spatio-spectral intensity profiles of the Bragg-diffracted beam at $y = 0$ simulated with the FFT-BPM method for the ideal crystal (center) and for the deformed crystal (right); color-scale units are arbitrary.

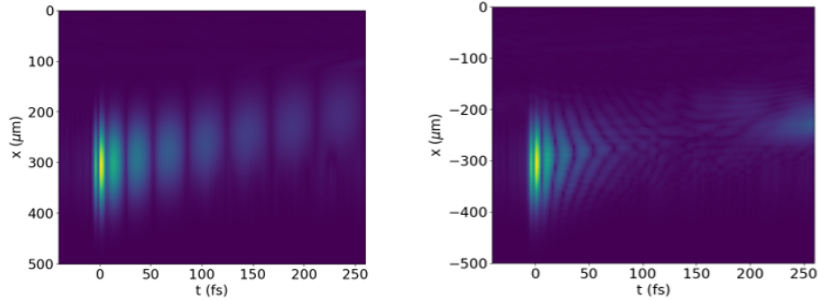


Figure 22. Spatio-temporal intensity profiles of the Bragg-diffracted and transmitted beam at $y = 0$ for the ideal crystal (left) and the deformed crystal (right); color-scale units are arbitrary.

The simulations shown in Fig. 21 and Fig. 22 were produced using the following Python scripts, configuration files, and Jupyter notebooks:

Left panel in Fig. 21:

- `SingleRealization_C400_ThermalBump.ipynb`
- `C400_TD_9p8keV_ThermalBump.yaml`

Central panel in Fig. 21 and left panel in Fig. 22:

- `run_parallel_TD_Not-deformed.py`
- `C400_TD_9p8keV_No-ThermalBump.yaml`
- `process-parallel-data-omegaC400-No-ThermalBump.ipynb`

Right panel in Fig. 21 and right panel in Fig. 22:

- `run_parallel_TD_deformed.py`

- `C400_TD_9p8keV_ThermalBump.yaml`
- `process-parallel-data-omegaC400-ThermalBump.ipynb`

Note that during a cross-check of the results published in Ref.,¹ Section “3.4 Time-dependent problems: deformed crystals,” we identified the following mistakes:

1. **Input pulse parameters:** The Gaussian pulse duration should be **2 fs**, and the RMS transverse size should be **60 μm** , instead of the previously stated **1 fs** and **30 μm** , respectively.
2. **Figure corrections (Fig. 8 in Ref.¹):** The maximum values on the vertical axis should be 8×10^{-5} , not 8×10^{-4} , and the plots should be **inverted with respect to the horizontal axis**.

9. SUMMARY

We have demonstrated that the Fast Fourier Transform Beam Propagation Method (FFT BPM) can be applied to simulate dynamic diffraction effects across a wide range of problems, including scattering from deformed crystals of any shape in Bragg, Laue, or asymmetric geometries. We successfully reproduced results presented in the literature for bent crystals, dislocations and crystals of finite shape simulated using the Takagi–Taupin equations.^{14–17}

Our FFT BPM method simplifies simulations compared to the TTE method by eliminating the need to solve boundary condition problems. This makes it well-suited for simulating scattering from finite crystals with arbitrary shapes and strain distributions, as well as illumination by X-ray beams with arbitrary angular spectral distributions (e.g., FEL SASE beams). The straightforward algorithm of the FFT BPM method is easy to implement in Python, and the use of FFT ensures fast computation. For instance, simulating 3D reflection from a strained 10 μm silicon cube on a $300 \times 200 \times 300$ rectangular grid, implemented in a Jupyter notebook and run on a single node of a high-performance computer, takes only a dozen seconds.

Our method can be naturally implemented on a multicore machine, where single realization reflection objects can be computed in parallel for different parameters, such as photon energy or incidence angle. This makes calculating a series of diffraction patterns by rotating the sample around the angular region near the Bragg peak or performing time-dependent diffraction an embarrassingly parallel problem.

Our compact FFT BPM Python code, with its straightforward implementation, can be easily shared with the X-ray community via GitHub. Here, we present a link to a GitHub repository² containing a Python code package for simulating the examples described in this article. These examples can be modified by adjusting the simulation parameters to address specific dynamical problems of interest in current research.

APPENDIX A. STANDARDIZED SIMULATION CONFIGURATION (75 PARAMETERS)

The following table provides a one-to-one mapping for the simulation parameters used in our FFT BPM Python package. Following our physical convention, Index 1 is assigned to the top film or surface layer, while Index 2 represents the substrate or bulk material.

Table 1. Complete Parameter Mapping for the 75-Parameter Master Template.

Category	Parameter	Description
Physics & Lattice	omega0, a0 Miller_h, k, l delta1, beta1 xrh1, xih1 delta2, beta2 xrh2, xih2	Photon energy (eV) and Lattice constant (Å). Reflection indices (H, K, L). Refractive index decrement and absorption (Film). Fourier susceptibility components (Film). Refractive index decrement and absorption (Substrate). Fourier susceptibility components (Substrate).
Grid & Geometry	xgrid, ygrid res_x, res_y xxmax, yymax asymm_angle thickness d_film width xs, x00 geometry geometry_file	Number of grid points in X and Y . Manual resolution overrides (0 = auto). Total simulation window dimensions (μm). Asymmetry angle (0° = Bragg, 90° = Laue). Substrate thickness (μm). Surface film thickness (μm). Finite crystal width (μm). Crystal lateral shift and global origin offset (μm). 'not_from_file', 'from_file', 'hemi-sphere'. Path to .npy file for arbitrary shapes.
Numerical Integration	M tpad Zstep_factor method, mode zsep	Number of integration steps along Z . FFT padding for wrap-around prevention. Step size stability multiplier. Integration method (Euler/Verlet) and mode (TIDP/TDP). Interval for saving Z -layers.
Beam Properties	beam, waist slit_x, slit_y time_dependent tgrid, tmax sigma_t	Beam profile type and FWHM/waist size (μm). Simulation slit dimensions (μm). 'None' or 'Temporal'. Number of time steps and total time range. Pulse duration (fs/fs).
Deformation & Dislocations	deformation strain, R vC100, vC, vSi x0d, y0d, z0d phid, burgers_vector def_amplitude def_period	Type (Bent Spectrometer, ScrewDislocation, etc.). Uniform strain and Bending radius (m). Poisson ratios for specific materials. Dislocation core coordinates (μm). Dislocation angle and Burgers vector components. Periodic deformation amplitude (Å). Periodic deformation period (μm).
Program Settings	nthread_fft quiet_mode store_fields	Number of CPU threads for FFT execution. Suppression of console output. Flag to save final electric field distributions.

ACKNOWLEDGMENTS

This work was supported by the U.S. Department of Energy (DOE) Contract No. DE-AC02-76SF00515 with SLAC.

REFERENCES

- [1] Krzywinski, J. and Halavanau, A., “Time-dependent dynamical Bragg diffraction in deformed crystals by the beam propagation method,” *Acta Crystallographica Section A* **78**, 465–472 (Nov 2022).
- [2] Krzywinski, J. and Halavanau, A., “Crystal-fft-bpm.” <https://github.com/balticfish/crystal-fft-bpm> (2022).
- [3] Hadley, G. R., “Wide-angle beam propagation using padé approximant operators,” *Opt. Lett.* **17**(20), 1426–1428 (1992).
- [4] Ersoy, O. K., [Diffracton, Fourier Optics and Imaging], John Wiley I& Sons, Ltd (2007).
- [5] Gaudin, J., Ozkan, C., Chalupský, J., Bajt, S., Burian, T., Vyšín, L., Coppola, N., Farahani, S. D., Chapman, H. N., Galasso, G., Hájková, V., Harmand, M., Juha, L., Jurek, M., Loch, R. A., Möller, S., Nagasano, M., Störmer, M., Sinn, H., Saksl, K., Sobierajski, R., Schulz, J., Sovak, P., Toleikis, S., Tiedtke, K., Tschentscher, T., and Krzywinski, J., “Investigating the interaction of x-ray free electron laser radiation with grating structure,” *Opt. Lett.* **37**(15), 3033–3035 (2012).
- [6] Andrejczuk, A., Krzywinski, J., and Bajt, S., “Influence of imperfections in a wedged multilayer laue lens for the focusing of x-rays investigated by beam propagation method,” *Nuclear Instruments and Methods in Physics Research Section B: Beam Interactions with Materials and Atoms* **364**, 60 – 64 (2015).
- [7] Morgan, A. J., Prasciolu, M., Andrejczuk, A., Krzywinski, J., Meents, A., Pennicard, D., Graafsma, H., Barty, A., Bean, R. J., Barthelmess, M., Oberthuer, D., Yefanov, O., Aquila, A., Chapman, H. N., and Bajt, S., “High numerical aperture multilayer laue lenses,” *Scientific Reports* **5**(1), 9892 (2015).
- [8] Bajt, S., Prasciolu, M., Morgan, A. J., Chapman, H. N., Krzywinski, J., and Andrejczuk, A., “One dimensional focusing with high numerical aperture multilayer laue lens,” *AIP Conference Proceedings* **1696**(1), 020049 (2016).
- [9] del Rio, M. S. and Dejus, R. J., “Xop v2.4: recent developments of the x-ray optics software toolkit,” *Proc. SPIE* **8141**, 8141 – 8141 – 5 (2011).
- [10] Authier, A., [Dynamical Theory of X-Ray Diffraction], International Union of Crystallography Monographs on Crystallography, Oxford University Press, Oxford (2003).
- [11] Omelyan, I., Mryglod, I., and Folk, R., “Optimized forest–ruth- and suzuki-like algorithms for integration of motion in many-body systems,” *Computer Physics Communications* **146**(2), 188–202 (2002).
- [12] Zhu, D., Cammarata, M., Feldkamp, J. M., Fritz, D. M., Hastings, J. B., Lee, S., Lemke, H. T., Robert, A., Turner, J. L., and Feng, Y., “A single-shot transmissive spectrometer for hard x-ray free electron lasers,” *Applied Physics Letters* **101**, 034103 (07 2012).
- [13] Kujala, N., Freund, W., Liu, J., Koch, A., Falk, T., Planas, M., Dietrich, F., Laksman, J., Maltezopoulos, T., Risch, J., Dall’Antonia, F., and Grünert, J., “Hard x-ray single-shot spectrometer at the European X-ray Free-Electron Laser,” *Review of Scientific Instruments* **91**, 103101 (10 2020).
- [14] Samoylova, L., Boesenberg, U., Chumakov, A., Kaganer, V., Petrov, I., Roth, T., Rüffer, R., Sinn, H., Terentyev, S., and Madsen, A., “Diffraction properties of a strongly bent diamond crystal used as a dispersive spectrometer for XFEL pulses,” *Journal of Synchrotron Radiation* **26**, 1069–1072 (Jul 2019).
- [15] Besedin, I. S., Chukhovskii, F. N., and Asadchikov, V. E., “Study of the diffraction contrast of dislocations in x-ray topo-tomography: A computer simulation and image analysis,” *Crystallography Reports* **59**, 323–330 (May 2014).
- [16] Kowalski, G. and Gronkowski, J., “On the intermediary image in x-ray section topography,” *physica status solidi (a)* **71**(2), 611–617 (1982).
- [17] Yan, H. and Li, L., “X-ray dynamical diffraction from single crystals with arbitrary shape and strain field: A universal approach to modeling,” *Phys. Rev. B* **89**, 014104 (Jan 2014).
- [18] “Perlmutter architecture.” <https://docs.nersc.gov/systems/perlmutter/architecture> (2026).
- [19] Shvyd’ko, Y. and Lindberg, R., “Spatiotemporal response of crystals in x-ray bragg diffraction,” *Phys. Rev. ST Accel. Beams* **15**, 100702 (Oct 2012).